Nanoparticles for PET Imaging of Tumors and Cancer Metastasis

Marie-Caline Z. Abadjian, Jaeyeon Choi, and Carolyn J. Anderson

1 Overview of PET Radionuclides and Chelation Chemistry

Positron Emission Tomography (PET) is a nuclear imaging modality that provides biochemical information with exquisite sensitivity for monitoring a variety of molecular processes using nM to pM concentration of radiotracers. PET imaging occurs after the administration of molecules labeled with radionuclides (typically called PET tracers or radiopharmaceuticals). The mass of PET tracer that is injected into the subject is extremely small (at the level of nmol to pmol), and causes minimal pharmacological effect. In this regard, PET enables the imaging and monitoring of disease in a noninvasive manner. PET has become a widely used diagnostic imaging tool by clinicians throughout the world. Although thousands of PET tracers have been developed for potential use in a clinical imaging setting, at present, only

M.-C. Z. Abadjian
Department of Medicine, University of Pittsburgh, 3501 Fifth Avenue, Pittsburgh, PA 15260, USA

Department of Radiology, University of Pittsburgh, Pittsburgh, PA, USA

J. Choi
Department of Bioengineering, University of Pittsburgh, Pittsburgh, PA, USA

C.J. Anderson, Ph.D. (✉)
Department of Medicine, University of Pittsburgh, 3501 Fifth Avenue, Pittsburgh, PA 15260, USA

Department of Radiology, University of Pittsburgh, Pittsburgh, PA, USA

Department of Bioengineering, University of Pittsburgh, Pittsburgh, PA, USA

Departments of Pharmacology and Chemical Biology, University of Pittsburgh, Pittsburgh, PA 15260, USA
e-mail: andersoncj@upmc.edu

J.W.M. Bulte, M.M.J. Modo (eds.), *Design and Applications of Nanoparticles in Biomedical Imaging*, DOI 10.1007/978-3-319-42169-8_11

Table 1 Decay characteristics of PET radionuclides for radiolabeling nanoparticles

Isotope	$T_{1/2}$	β^- MeV (%)	β^+ MeV (%)	EC (%)	γ MeV (%)
^{18}F	110 min	–	0.634 (97%)	3%	0.511 (194%) 1.66 (3.1%)
^{64}Cu	12.7 h	0.573 (38.4%)	0.655 (17.8%)	43.8%	0.511 (35.6%) 1.35 (0.6%)
^{68}Ga	68 min	–	1.90 (87.7%) 0.82 (1.2%)	11%	0.511 (178%)
^{89}Zr	78.4 h	–	0.902 (22.8%)	77.2%	0.511 (45.6%) 0.909 (99%)
^{124}I	100.2 h	–	1.54 (11.7%) 2.14 (10.8%)	77%	0.511 (45%) 0.603 (63%) 1.69 (10.9%) 0.723 (10.4%)

a handful (including [^{18}F]-labeled 2-fluorodeoxyglucose (FDG) and three Alzheimer's disease agents) are approved for routine clinical evaluation. Small animal PET systems for rodent imaging with 1–2 mm resolution are used to evaluate PET tracers in mouse and rat models to evaluate their suitability for humans.

1.1 Positron-Emitting Radionuclides

Traditional positron-emitting radionuclides include short-lived isotopes such as fluorine-18 (^{18}F; $T_{1/2}=110$ min), carbon-11 (^{11}C; $T_{1/2}=20$ min), nitrogen-13 (^{13}N; $T_{1/2}=10$ min), and oxygen-15 (^{15}O; $T_{1/2}=2$ min). Nontraditional positron-emitting radionuclides, particularly those of the transition metals, have gained considerable interest for imaging with PET because of increased production and availability (Table 1). For example, radionuclides of copper (^{64}Cu; $T_{1/2}=12.7$ h) and zirconium (^{89}Zr; $T_{1/2}=78.4$ h) allow radiolabeling of agents that clear the blood circulation more slowly [1].

1.2 Chelation Chemistry

The most commonly used chelators for complexing ^{64}Cu to nanoparticles are tetraazamacrocyclic ligands with pendant arms. The chelators DOTA (1,4,7,10-tetraazacyclododecane-1,4,7,10-tetraacetic acid), NOTA (1,4,7-triazacyclononane-1,4,7-triacetic acid), and TETA (1,4,8,11-tetraazacyclotetradecane-1,4,8,11-tetraacetic acid) have been the most widely used in ^{64}Cu-labeled nanoparticles, with DOTA being the most popular (Fig. 1). Anderson and colleagues have shown that cross-bridged macrocycles form more kinetically stable ^{64}Cu(II) complexes in vivo [2]; however, it has been demonstrated that there are only

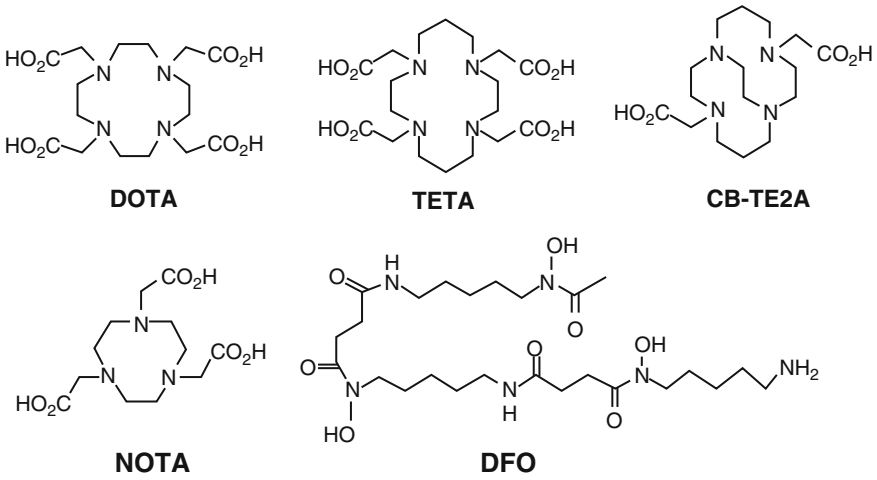

Fig. 1 Chelators that have been employed for complexing radiometals to nanoparticles

minimal differences in mouse biodistribution between DOTA and CB-TE2A conjugates of micellular nanoparticles [3]. Although the development of stable chelators for ^{89}Zr is an active area of research [4, 5], thus far, the chelator deferrioxamine (DFO) is the chelator of choice for attaching ^{89}Zr to nanoparticles. Examples of the nanoparticles labeled with radiometal chelates will be provided in the forthcoming sections.

2 Silica-Based Nanoparticle PET Tracers

Silica-based nanoparticles that have been employed in PET imaging are typically modified forms of mesoporous silica or coated dense silica nanoparticles ($dSiO_2$). Since the late 1990s, mesoporous silica nanoparticles (MSNs) have been studied extensively for a variety of applications due to their biocompatibility, large surface areas and ease of surface modification [6–9]. Various groups have coupled targeting moieties, drugs, and imaging agents to MSNs to investigate them as efficiency delivery vectors to tumors (Fig. 2) [10, 11].

MSNs also experience the EPR effect when their diameter is 100–130 nm making them suitable for imaging tumors [12]. For example, aza-dibenzocyclooctyne (DBCO) PEGylated MSNs have been coupled via a biorthogonal in vivo click reaction to ^{18}F-labeled azides to give ^{18}F-DBCO-PEG-MSNs (~150 nm) (Fig. 2c) [13, 14]. This study investigated these PET agents in female nude mice bearing subcutaneously (s.c.) U87MG tumors (Fig. 3). The DBCO-PEG-MSNs were injected in mice 24 h before the ^{18}F-labeled azide, allowing the MSNs to accumulate in the tumors prior to giving the ^{18}F-azide, which would allow localization of ^{18}F to the tumor, and clearance of all unreacted ^{18}F-azide.

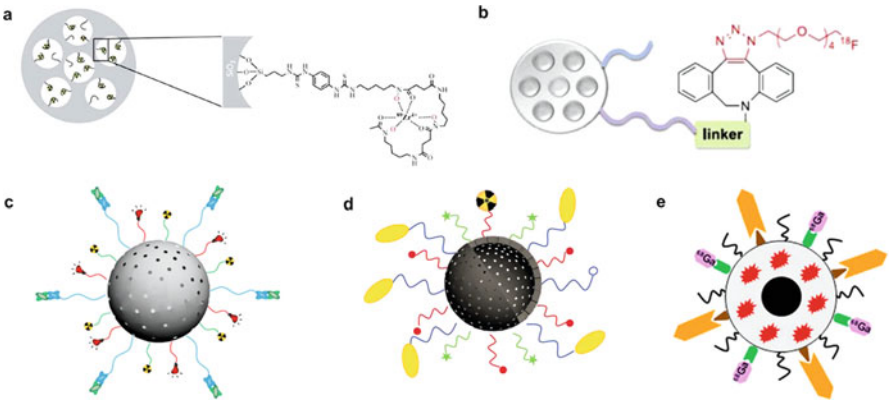

Fig. 2 Silica-based nanoparticles PET tracers: (**a**) representation of MSNs functionalized with APTMS, coupled with DFO-NCS and radiolabeled with radionuclide ^{89}Zr [15]; (**b**) ^{18}F-labeled peptide radiotracers [14]; (**c**) ^{64}Cu-MSN-800CW TRC105(Fab) [16]; (**d**) ^{64}Cu-NOTA-HMSN-fluorecein-PEG-cRGDyK nanoconjugate for drug delivery studies [18]; (**e**) ^{68}Ga was labeled with the MF-uMUC-1 [17]

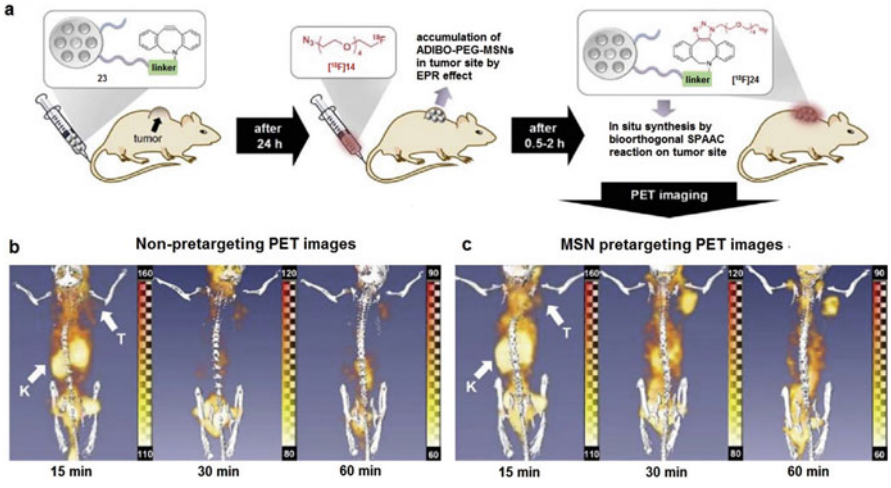

Fig. 3 Pretargeting PET imaging study by bioorthogonal covalent ^{18}F-labeling. (**a**) The procedure for the in situ synthesis of ^{18}F -DBCOT-PEG- MSNs in a living specimen by a bioorthogonal SPAAC reaction for the DBCO-PEG-MSN-pretargeting PET-imaging study. Three-dimensional reconstruction (*upper*) and transverse section (*lower*) combined PET-CT images of ^{18}F-labeled azide ([^{18}F]2 ; 2.6 MBq) in a U87 MG tumor-bearing mouse given only [^{18}F]2 alone (non-pretargeted ; (**b**) or a mouse given DBCO-PEG-MSNs 24 h earlier (pretargeted ; **c**) recorded at 15, 30, 60, and 120 min after injection of [^{18}F]2. *T* tumor, *K* kidneys [13]

PET images of the clicked MSNs in tumor were observed 2 h postinjection (p.i.) of the azide. Another group designed a new ^{89}Zr desferrioxamine (DFO) MSNs (~180 nm) to image SCID mice with s.c. prostate carcinoma cell lines (LNCaP and C4-2) finding minimal dissociation of $^{89}Zr^{4+}$ and typical biodistribution compared to other PET MSNs (Fig. 2a) [15].

MSNs can accommodate various surface modifications making them multimodality imaging agents not only for PET, but also near infrared fluorescence (NIRF) imaging and MRI. The surface of these nanoparticles can also be coupled to targeting agents. PET/ NIRF MSNs were developed with vasculature targeting capability to image 4 T1 murine breast cancer tumors in mice (Fig. 2d) [16]. Surface coupling of a human/murine chimeric IgG1 monoclonal antibody (TRC105(Fab)), NIR dye (800CW), and ^{64}Cu-NOTA labeling resulted in MSNs (175.3 ± 9.7 nm) imaging tumors with 5.4 ± 0.2 % ID/g at 4 h p.i.. Another example of multimodality silica NPs was comprised of PET, NIRF, MRI agents and a targeting moiety that successfully imaged BT-20 cells in a nude mouse model (Fig. 2f) [17]. The silica-based nanoparticles (81 nm) have a cobalt ferrite core with rhodamine B in the silica shell and surface coupled underglycosylated mucin-1 antigen (uMUC-1 aptamer), along with NOTA for Ga-68 labeling.

Targeting of tumors has also been shown in hollow mesoporous silica nanoparticles (HMSNs) in U87MG tumor-bearing female athymic nude mice (Fig. 2e) [18]. Dense silica nanoparticles coated with MSNs have surface coupled cyclic arginine-glycine-aspartic acid (cRGDyK) peptide, ^{64}Cu-NOTA as well as anticancer drug (Sunitinib) loaded in the core. PET images showed relatively high uptake (7.2 ± 0.6 % ID/g) at 0.5 h postinjection.

3 Gold Nanoparticle (AuNP) PET Tracers

Gold nanoparticles (AuNPs) are a promising platform for biomedical applications and have rapidly advanced toward multifunctional particles for imaging and treatment of cancer. AuNPs have been at the forefront of cancer research in recent years owing to the high biocompatibility via functionalization, their low toxicity of the gold core, and availability in a range of sizes and shapes [19, 20].

The readers are referred to a highly comprehensive review by Daniel and Astruc for information on the structure and properties of AuNPs [21]. Surface plasmon resonance (SPR), a unique plasmatic absorption band phenomenon of AuNPs, can be converted to strong infrared spectral ranges, thereby allowing vital optical imaging in tissues where light exhibits minimal absorption and deep penetration in tissue. These specialized properties have also been used for photothermal therapy, which is a noninvasive, accurately targeted hyperthermia cancer treatment based on the optical absorbance of AuNPs in the intrinsic near-infrared (NIR) (650–900 nm) [22]. AuNPs also provide attractive scaffolds for many biomedical imaging modalities, including surface-enhanced Raman scattering (SERS), two-photon photoluminescence (TPL), magnetic resonance imaging (MRI), positron emission tomography (PET), and X-ray computer tomography (CT) imaging [23, 24].

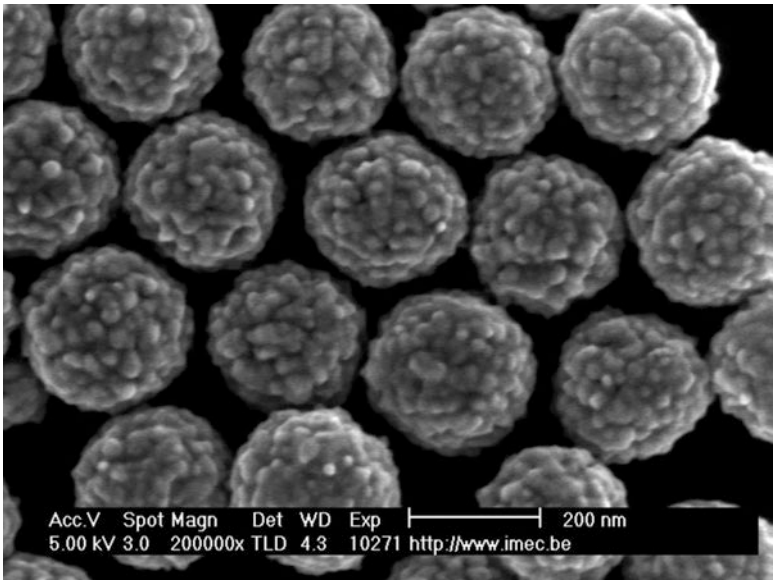

Fig. 4 SEM image of a monolayer portion showing self-assembled silica/gold nanoshells on a silane functionalized quartz substrate [25]

3.1 Types of AuNPs

Typically, the dual imaging AuNPs are synthesized from commercial HAu_3Cl_4 by the reduction of Au^{3+} ions to metallic Au atoms (Au^0) using citrate ions as a reducing and capping agent. There are different types of gold nanoparticles in the size range of 9–120 nm that have been developed with various shape, size, and physical properties (Fig. 4) [25].

Gold nanosheres (gold colloids) in the size range of 2–100 nm can be produced by chemical reduction of gold chloride, with the properties controlled by citrate/gold ratio. The absorption spectra of gold nanospheres (visible range of 510–550 nm) are related to the size distribution [26–28].

Gold nanorods are synthesized by a special template method based on the electrochemical deposition of gold within the cylindrical pores of rigid matrices, such as nanoporous polycarbonate or alumina template membranes. Gold nanorods have absorption and scattering peaks that can be converted to the visible and near IR spectra, generating heat when excited by IR light. The characteristic has been widely applied to selectively destroy cancer cells [29].

Nanoshells, silica coated nanoparticles with a thin film of gold, have been used for an optical imaging with SPR in the visible to the NIR region [30, 31].

Gold nanocages are synthesized by reacting silver nanoparticles with chloroauric acid in aqueous conditions, and range in size from 10 to 150 nm. As the optical resonance peaks shift to near-infrared light, the strong absorption of gold nanocages enhances the contrast and photothermal effect for cancer diagnostic and therapy [32, 33].

3.2 Radiolabeling Chemistry of AuNPs

The surface of AuNPs can be modified with ligands, surfactants, polymers, and dendrimers. Upon functionalizing with thiol groups that strongly bind with gold, AuNPs can be readily conjugated to chelators or targeting molecules [34], enabling the conjugation of biofunctional chelates such as 1,4,7-triazacyclononane-1,4,7 -triacetic acid (NOTA) or 1,4,7,10-tetraazacyclododecane-1,4,7,10-tetraacetic acid (DOTA) via a thiol-maleimide coupling chemistry. Bifunctional chelators play an important role in conjugation of metal radionuclides on the AuNPs surface. For example, Gd^{3+} is attached on a chelate on the AuNPs surface for MRI imaging, whereas for PET imaging, radionuclides such as ^{64}Cu, ^{68}Ga, and ^{89}Zr are generally used for PET/MR tracers. Targeting molecules added to the surface of AuNPs can render them tumor-specific for targeting via receptors expressed exclusively on target cancer cells, improving tumor localization over the nonspecific enhanced permeability and retention effect (EPR) [35].

^{64}Cu-labeled RGD peptide-gold nanoshells (^{64}Cu-NS-RGDfK) were developed for targeting integrin $\alpha_v\beta_3$ on tumor cells. The NSs were conjugated with RGDfK and DOTA through bifunctional PEG, and the surface modified size was ~170 nm. PET/CT imaging of two rats bearing head and neck xenografts showed high tumor uptake beginning at 4 h postinjection and reaching a maximum at 20 h, with a decrease in tumor accumulation until 44 h postinjection [36].

Nonchelator conjugated [^{64}Cu]CuS AuNPs (11 nm) was developed for a tumor theranostic probe both for PET imaging and as photothermal ablation agents using a passive targeting strategy in a breast cancer mouse model. At 24 h, biodistribution in mice bearing subcutaneous U87 glioma xenografts showed that the PEG-[^{64}Cu]CuS NPs reduced liver/spleen uptake and enhanced tumor uptake ratio (7.6 ± 1.4 %ID/g) [37].

Other chelate-free ^{64}Cu-labeled alloyed AuNPs (27 nm hydrodynamic (HD) size) were developed for cancer imaging. In these AuNPs, ^{64}Cu is directly incorporated into the lattice of the gold nanoparticle structure, maintaining high stability in vivo. The PET/CT image using EMT-6 tumor-bearing mouse showed 4.93 ± 0.32 % ID/g of tumor uptake ratio at 1 h of postinjection, increasing at 48 h pi to 16.8 ± 0.98 %ID/g, with a tumor/muscle ratio of 16.2 ± 1.07 [38]. However, there was very high liver and spleen uptake of these particles at 48 h postinjection (~45 % ID/g liver and ~200 %ID/g spleen), (Fig. 5). The surface of these $^{64}CuAuNCs$ was then PEGylated with different-sized PEG chains (^{64}Cu-labeled AuNCs-PEG350, HD size of 4.3 nm vs. AuNCPEG1000, HD size of 6.9 nm) [39]. Biodistribution in PC3 tumor-bearing mice showed that both particles had dramatically decreased spleen uptake at 48 h (5 % ID/g or less), and the liver uptake was also <20 % ID/g. There was also significantly lower tumor uptake (3–5 % ID/g) for both sized AuNCs, with tumor:muscle ratios ~2.5 [38].

^{64}Cu-labeled hollow gold nanospheres (HAuNS) showed differential tumor uptake after hepatic intra-arterial (IA) and intravenous (IV) injection in VX2 liver tumor-bearing rabbits. RGD-PEG-HAuNS had an average diameter of ~40 nm. A DOTA analog chelator was attached to RGD-PEG-HAuNS for radiolabeling with Cu-64. PEG-HAuNS with lipiodol (IA-PEG-HAuNS-lipiodol) after hepatic

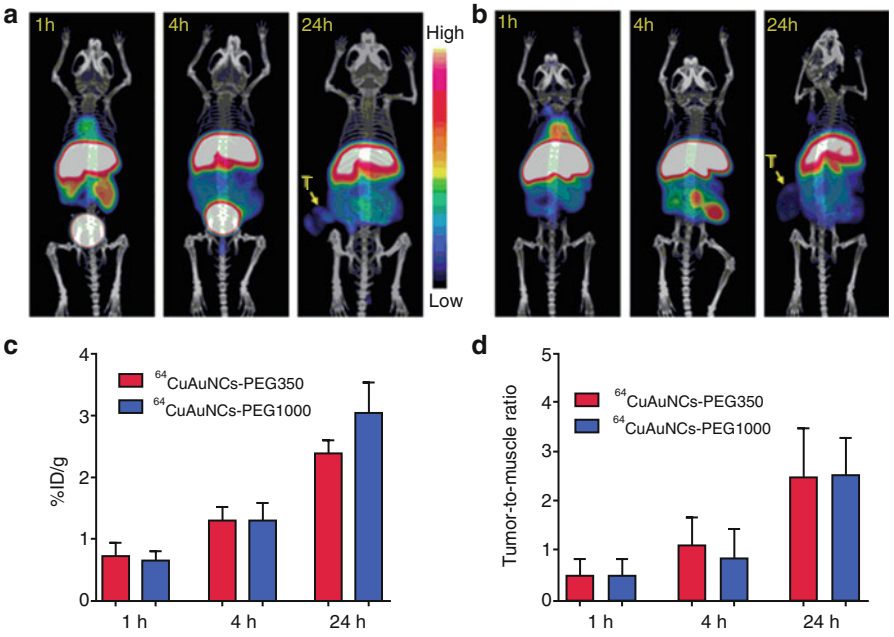

Fig. 5 PET/CT images at 1, 4, 24 h postinjection of ^{64}Cu-AuNCs-PEG350 (**a**) and ^{64}Cu-AuNCs-PEG1000 (**b**) in PC3 prostate-tumor-bearing mice. Quantitative tumor uptake (**c**) and tumor:muscle ratios (**d**) of the two agents (38)

intra-arterial injection had the highest tumor uptake (0.3319 ± 0.0711 ID%/g) compared to that of other ^{64}Cu-labeled PEG-HAuNS and ^{64}Cu radiolabeled RGD peptide-HAuNS after IA and IV injection, respectively. The result showed that adding iodized oil to PEG-HAuNS group can increase delivery of nanoparticles to hepatic tumors [40].

An RGD peptide was coupled with Gd-chelate coated gold nanoparticle (Au@DTDTPA-RGD) and labeled with ^{68}Ga for a dual PET/MRI imaging modality targeting integrin $\alpha_v\beta_3$ receptor-positive U87MG cancer cells. Biodistribution studies showed that the tumor to muscle ratio increased from 1 to 2 h postinjection (3.71 ± 0.22 and 4.69 ± 0.09 respectively) [41].

^{89}Zr-labeled anti-CD105 was coupled with gold nanoparticles (^{89}Zr-anti-CD105-AuNPs-PPAA), having a mean diameter of 102.6 ± 4.0 nm. Two groups of B16 melanoma-bearing mice were injected with ^{89}Zr-Df-Bz-NCS-anti-CD105 antibody or with ^{89}Zr-anti-CD105-AuNPs-PPAA, respectively. The similar PET imaging pattern was observed, but ^{89}Zr-anti-CD105-AuNPs-PPAA had higher uptake in liver, spleen, and lung compared to that of ^{89}Zr-Df-Bz-NCS-anti-CD105 antibody due to its large size of the nanoparticle. The biodistribution study between ^{89}Zr-anti-CD105-AuNPs-PPAA and ^{89}Zr-Df-Bz-NCS-anti-CD105 showed that no significant differences in tumor:background ratios were observed [42].

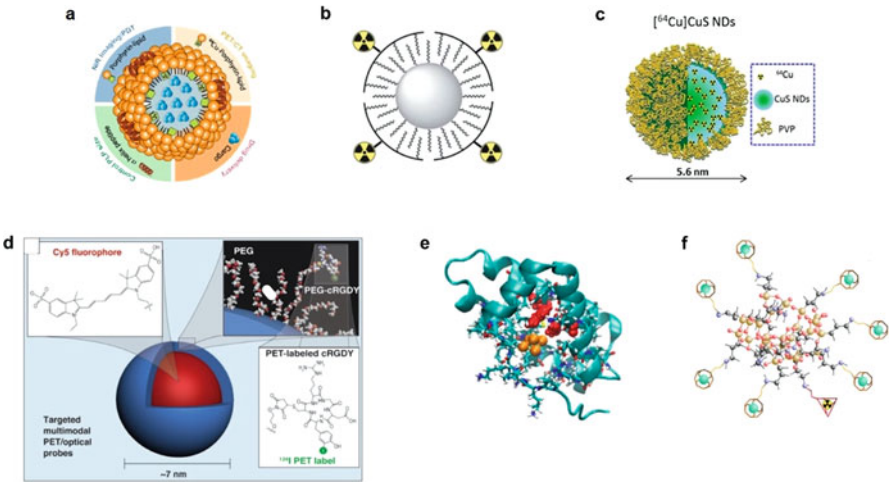

Fig. 6 Ultrasmall nanoparticles: (**a**) PLP structure [51]; (**b**) USPIO@OPA [52]; (**c**) [^{64}Cu]CuS ND [53]; (**d**) C dots [54]; (**e**) [^{64}Cu]CuNC@BSALHRH [56, 57]; (**f**) AGuIX nanoparticles [58]

4 Ultrasmall Nanoparticle PET Tracers

Ultrasmall nanoparticles are defined by their size (less than 10 nm), falling within the renal glomerular filtration size cutoff (~10 nm) [43–46]. Nanoparticles that fall between 10 and 200 nm are known to accumulate in the reticuloendothelial system (RES), which includes the liver, lymph nodes, bone marrow, and spleen, leading to longer retention in the body that could cause long-term adverse effects [47–50]. Small nanoparticles (~10–100 nm) and ultrasmall nanoparticles have unique properties, sparking interest in targeted therapies using PET imaging. Small and ultrasmall nanoparticles have provided biocompatible vectors compact enough to study metabolic pathways and therapies (Fig. 6). Some small nanoparticles mimic lipoprotein structures to sustain longer circulation as an alternative to PEGylation. A porphylipoprotein (PLP) nanoplatform (20.6 ± 5.2 nm) has been developed for fluorescence imaging and photodynamic light therapy of glioblastoma multiforme (Fig. 6a) [51]. PET imaging using ^{64}Cu-labeled versions of PLP and PEGylated PLP in SKOV3 orthotopic ovarian cancer model showed similar uptake in tumors, but striking differences in spleen uptake, 3.4 ± 0.2 % ID/g versus 19.8 ± 1.6 % ID/g, respectively. Other compositions of similar sized nanoparticles like ultrasmall superparamagnetic iron oxide nanoparticles (USPIOs) have also been studied for their biocompatibility and cellular uptake effi ciency (Fig. 6b) [52]. USPIOs were coated with octylamine-modified polyacrylic acid (OPA) (10 ± 2 nm) and conjugated with a ^{64}Cu chelator (DMPTACN) for PET imaging of mice bearing tumors of various human cell lines (epidermoid carcinoma A431, squamous cell carcinoma FaDu, ductal carcinoma MDA-MB 435S, umbilical vein endothelial HUVEC), finding generally low toxicity.

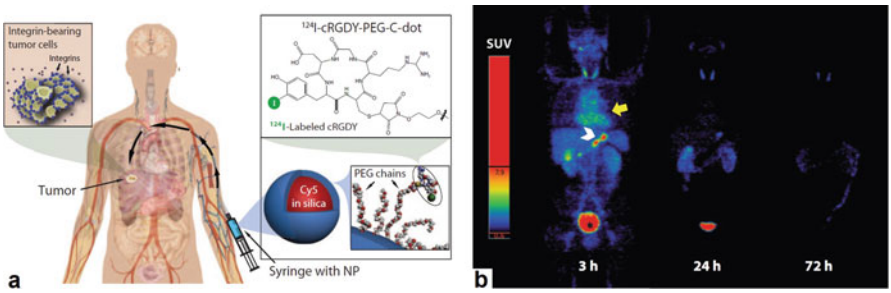

Fig. 7 (**a**) Cornell dots (C dots) conjugated with ^{124}I-labeled cRGDY have been investigated in humans with cancer for safety, biodistribution, and dosimetry; (**b**) PET image in patient #3 showing activity in bladder, heart, and bowel [55]

Nanodots also fall into the category of ultrasmall nanoparticles and have shown interesting applications as photothermal agents and in tumor imaging. Copper-64 labeled copper sulfi de nanodots ([^{64}Cu]CuS NDs) coated with polyvinylpyrrolidone (~5.6 nm) were found to have tumor uptake in 4 T1 tumors in Balb/c mice (3.62 ± 0.50 % ID/g, 2 h p.i.) and fast renal clearance (Fig. 6c) [39, 53]. Cornell dots (C dots) are ultrasmall inorganic optical-PET imaging nanoparticles probes. The silica-based core contains encapsulated Cy5 fluorophore and the surface is PEG-coated with conjugated 124 I-labeled cyclic arginine-glycine-aspartic acid (cRGD, for αvβ3 integrin targeting) (Fig. 6d) [54]. The C dots were found to have high receptor-binding specificity, and biodistribution and targeting kinetics data, clearance and dehalogenation profiles, blood/tissue residence times, and bioavailability and radiation dosimetry were reported (Fig. 7). This ultrasmall nanoparticle has received FDA-approval for a first-in-human clinical trial and found to be safe in human (five patients) as a diagnostic for metastatic melanoma [55]. The preliminary trial found that the agent was well tolerated, cleared quickly from the body through the kidneys, and the 124 I-label was stable in vivo. Two patients showed tumor uptake in a pituitary and a liver lesion. To date, this is one of the few nanoparticle-based PET tracers to be evaluated in human cancer patients. Some ultrasmall nanoparticles are small enough to be considered clusters or matrices. One group has made chelator-free labeled [^{64}Cu]Cu nanoclusters coated with bovine serum albumin (BSA) for PET imaging for tumors (Fig. 6e) [56, 57]. These nanoclusters have been conjugated with a tumor target peptide, lutenizing hormone releasing hormone (LHRH), giving [^{64}Cu]Cu NC @BSA-LHRH (3.8 ± 0.5 nm) that were studied in mice bearing orthotopic A549 lung tumors (Fig. 8). The targeted nanoclusters were found to have much higher tumor uptake 12 % ID/g than nontargeted 3 % ID/g at 4 h p.i. Other interesting ultrasmall nanoparticles were made from a polysiloxane matrix coated with chelators for PET/MR dual imaging [58]. These ultrasmall nanoparticles (AGuIX) are only 2.5 ± 0.1 nm in diameter (Fig. 6f). They have been well-characterized and have shown no toxicity in U87MG (human primary glioblastoma) and HEKβ3 (human embyonic kidney) cell lines.

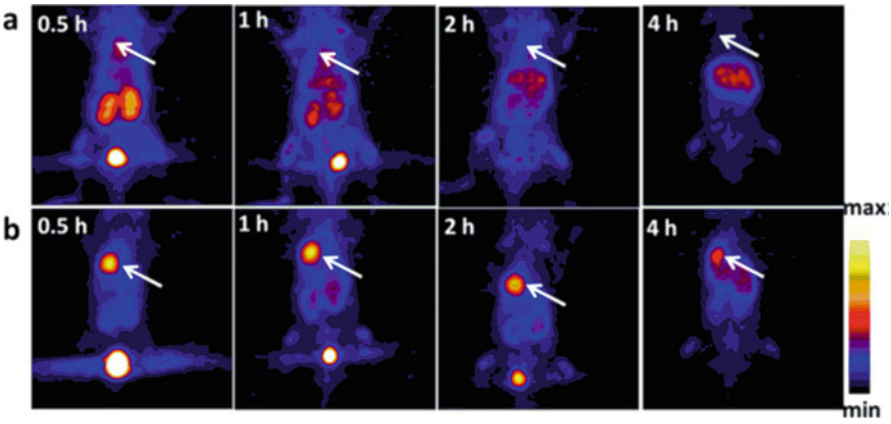

Fig. 8 Representative PET images of coronal single slices on orthotopic A549 lung tumor-bearing mice after intravenous injection of 6.7 MBq of [^{64}Cu]CuNC@BSA (**a**) and [^{64}Cu]CuNC@BSA-LHRH (**b**). Images were acquired at 0.5, 1, 2, and 4 h. White arrows indicate the lung tumor [57]

PET/CT imaging using ^{68}Ga-labeled AGuIX was found to have rapid clearance and coherence with MR images. The development of ultrasmall nanoparticles is becoming a new avenue for targeted imaging and therapy.

5 Radiolabeled Iron Oxide Nanoparticles (IONPs)

Iron oxide particles have been widely studied as an excellent MRI contrast agent in clinical trials due to its ideal paramagnetic and low toxicity [59, 60]. MR imaging is optimized with functional parameters such as spin-lattice relaxation time (T1) and spin–spin relaxation time (T2), which are a function of the local chemical structure of the molecules being imaged. The core of iron oxide particles is composed of iron and oxygen atoms, generating mostly magnetite (Fe_3O_4), magnemite, (γ-Fe_2O_3), and hematite (α-Fe_2O_3), which exhibit superparamagnetic physical properties at ambient temperature if the core diameter is relatively small (<20 nm) [61–63]. Iron oxide nanoparticles (IONPs) have a number of advantages for multimodality (e.g., PET/MRI) imaging: 1) they can be modified on the surface for conjugation with a large number of targeting ligands, thus enhancing the biological specificity and affinity to targeted molecules; 2) the nanoparticles can be coupled with chelators for labeling with metal radionuclides for PET or SPECT imaging; and 3) iron oxide nanoparticles can circulate in the blood vessels for a relatively long time, moving larger amount of radionuclides or other cargo to targeted organs [64]. *Please see Chap. 10 for more detailed information on structural properties of IONPs.*

^{64}Cu-DOTA-RGD-conjugated IONPs were developed for targeting tumor $\alpha_v\beta_3$ integrin. Polyaspartic acid (PASP)–coated iron oxide was coupled with RGD and DOTA via surface amino groups for ^{64}Cu-labeling. The hydrodynamic diameter is

45 ± 10 nm. In vivo PET studies in U87MG tumor-bearing mice showed tumor imaging at 1 h (7.9 ± 0.8 %ID/g), 4 h (10.1 ± 2.1 %ID/g), and 21 h (9.8 ± 3.2 %ID/g), respectively, after injection of ^{64}Cu-DOTA-iron oxide-RGD [65].

^{89}Zr-Deferoxamine-RGD-IONP, another RGD-iron oxide, was developed targeting $\alpha\nu\beta3$ and $\alpha\nu\beta5$ integrins overexpressed in nascent endothelial cells during angiogenesis in various tumors, but not in inactive endothelial cells. The PET/CT and MRI imaging after intravenously injection in tumor-bearing mice showed high accumulation in the liver and spleen at 1 h after injection, which remained high at subsequent time points. After 24 h, accumulation in tumor was observed with persistent and intense signal until 72 h, clearly delineating the tumor [66].

Protein-based ligands, such as affibodies, have been investigated as tumor targeting agents. An anti-EGFR affibody was conjugated to Au-Iron Oxide NPs (NOTA-Au-IONP-affibody) having an average size 24.4 ± 2.0 nm, and was labeled with ^{64}Cu. An in vitro study showed that NOTA-Au-IONP-Affibody probes had a higher cellular uptake in EGFR-positive tumor A431 cells at 1 and 2 h time points, respectively, compared with blocking samples (Fig. 9). The small animal PET images showed high tumor accumulation (4.6 % ID/g at 24 h p.i.), and high tumor-to-normal tissue contrast for ^{64}Cu-NOTA-Au-IONP-affibody. The biodistribution studies also indicated that the nanoprobe had higher tumor uptake value compared to the blocking group [67].

6 Liposome-Based PET Agents

Liposomes used in PET imaging are an attractive vector for imaging tumors and diseased tissues, as well as drug targeting. The study of liposomes as imaging agents started in the late 1980s [68], although it was not until the late 1990s that liposomes were radiolabeled for imaging purposes [69–72]. Generally, liposomes are lipid vesicles formed from thin lipid films or cakes. Upon hydration, layers of the bilayer sheets self-assemble into multilamellar vesicles (MLVs) where the hydrophilic portions face the water surrounding and within the vesicles. The size of these liposomes can then be reduced to unilamellar vesicles by input of either sonic energy (sonication) or mechanical energy (extrusion). Liposomes are typically characterized by their particle size (dynamic light scattering), zeta potential (laser doppler microelectrophoresis), and uniform size distribution. Like all nanoparticles used in medicine, the size and charge of the nanoparticle play a big role in their fate in vivo. Most liposomes range in size from 90 to 925 nm and are either negatively charged or neutral. This size range is meant to be above the renal threshold for longer circulation.

The success of liposomes in clinical and investigational research has led researchers to combine the physiological properties of liposomes with the quantitative imaging capability of PET. The longer-lived PET radionuclides (^{64}Cu, ^{62}Cu, ^{124}I, ^{89}Zr) have been typically investigated with liposomes to take advantage of the EPR effect; however, shorter-lived radionuclides (^{11}C, ^{18}F, ^{15}O) have also been studied for PET imaging [73]. Incorporating a radionuclide for PET imaging into a liposome can be achieved by (1) encapsulation; (2) remote loading (after-loading); (3) bilayer chelation; or (4) surface chelation.

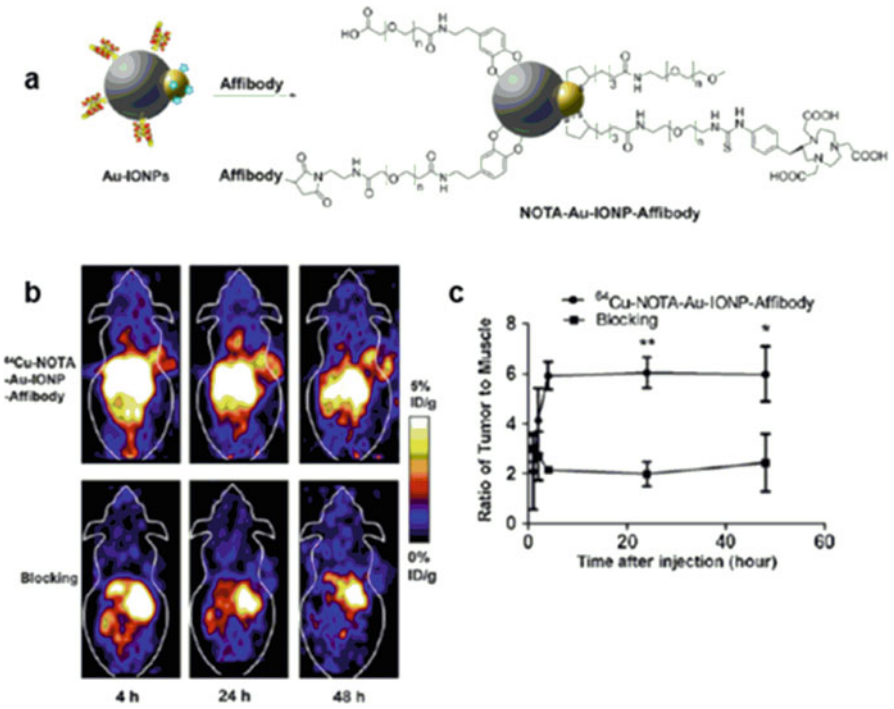

Fig. 9 (**a**) Schematic illustration of Affibody binding domain with Au-IONP and its functionalization and conjugation with affibodies and the NOTA chelator; (**b**) PET image of A431 tumor-bearing mice at 4, 24, and 48 h postinjection of ^{64}Cu-NOTA-Au-IONP-Affibody, with and without blocking; (**c**) tumor:muscle ratios with and without blocking [67]

A ^{18}F-labeled cholesteryl ether (^{18}FCE) PEGylated liposome employed bilayer chelation to incorporate radioactive lipophilic labels in the liposome membrane (Fig. 11a) [74]. The liposome ^{18}FCE was found to accumulate in NCI-H727 human lung carcinoid tumors of tumor-bearing nude mice after 8 h (2.25 ± 0.23 %ID/g). Another ^{18}F-labeled liposome (^{18}F-TCO-liposome) incorporated the fast tetrazine (Tz)/*trans*-cyclooctene (TCO) inverse electron demand Diels-Alder cycloaddition (IEDDA) and pH (low) insertion pepide (pHLIP) to speed up tumor accumulation (Fig. 11b) [75]. Tumor-bearing athymic nude mice were injected with SKOV3 ovarian cancer cells and pHLIP-Tz (Fig. 10). The ^{18}F-TCO-liposome could be detected as early as 30 min after injection of the liposome. After 120 min, tumors marked with pHLIP-Tz had higher activity (3.5 ± 1.2 %ID/g) compared to tumor without pHLIP-Tz (0.46 ± 0.04 %ID/g).

For longer circulating PET imaging agents, Zr-89 is favored due to its half-life (78.4 h) and relatively lower fraction of gamma radiation than ^{124}I and ^{86}Y [76, 77]. Several groups have utilized the combination of the liposome's EPR effect over time and ^{89}Zr as a PET imaging agent. ^{89}Zr-PEGylated-liposomes radiolabeled by surface chelation have shown tumor accumulation peaks at 24–48 h postinjection

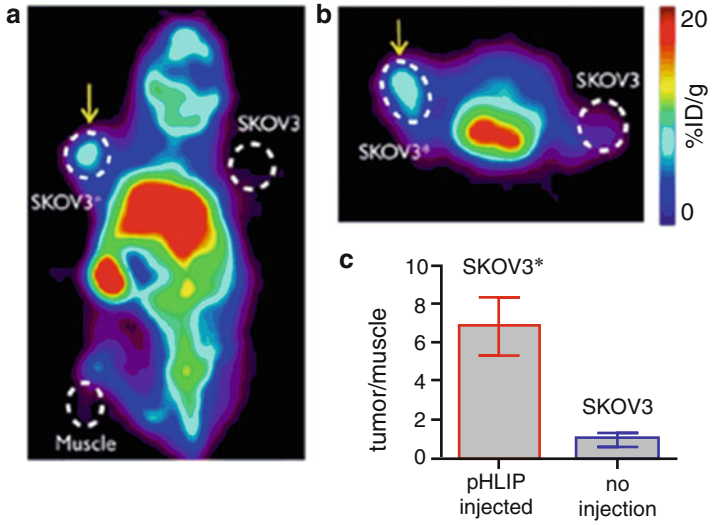

Fig. 10 Biodistribution and PET imaging of bioorthogonal ^{18}F-liposomes as a selective marker for tetrazine-labeled SKOV3 ovarian cancer xenografts. (**a**, **b**) PET imaging at 2 h postinjection in a mouse bearing both pHLIP-Tz-treated (SKOV3, left shoulder, *yellow arrow*) and untreated (SKOV3 right shoulder) tumors. Normalized tumor:muscle ratios for treated and untreated tumors at 2 h post-injection [75]

(Fig. 11c) [78, 79]. The PEG groups on the surface of the liposomes assist with longer circulation, giving the liposomes time to accumulate in/around tumors. Another ^{89}Zr-PEGylated-liposome also included a targeting agent, octreotide, on the surface of the liposome (OL) (Fig. 11d) [80]. Octreotide is a peptide targeting human somatostatin receptor subtype 2 (SSTr2) found on tumor cells. The ^{89}Zr-Gd-OL imaging agent was found to specifically accumulate at the tumor site at 50 h postinjection.

Other radionuclides, especially Cu-64, have gained attention as a viable radionuclide coupled to liposomes for PET imaging. Several groups have used Cu-64 with their liposomes to study a variety of tumor models. Remote loading and surface chelation are some of the more common methods for radiolabeling liposomes. Remote loading using 2-hydroxyquinoline has been shown to be highly efficient compared to other ionophores [81]. Unassisted radiolabeling or remote loading without the use of ionophores has shown evidence of similar radiolabeling efficient compared with ionophores (Fig. 11f) [82]. Copper-64 has been remotely loaded into liposomes containing surface targeting SSTr2 in human neuroendocrine carcinoma in mouse models (Fig. 11g) [83] and mannose-coated liposomes targeting macrophages in the tumor microenvironment (TME) [84]. Surface chelation and modification using ^{64}Cu has yielded informative findings in tumor targeting and organ uptake. DOTA and TETA macrocycle analogs have been used to coordinate the radionuclides to the liposome giving a stable radiolabeled liposome (Fig. 11e) [85, 86].

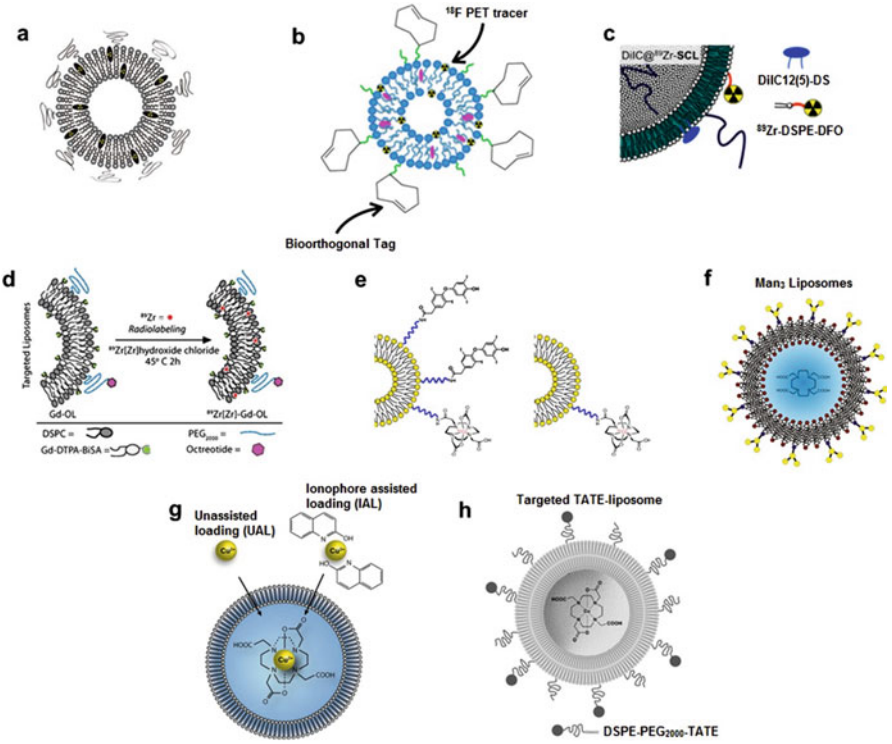

Fig. 11 Liposome-based PET agents: (**a**) PEGylated liposome incorporating radioactive lipophilic labels in the membrane [74]; (**b**) ^{18}F-TCO-liposomes and pHLIP-Tz coupling for pretargeting of acidosis [75]; (**c**) dual-labeled liposome DiIC@89Zr-SCL [78]; (**d**) OCT was conjugated to preformed Gd-Control LPs (CL) resulting in targeted OCT-LP (OL) [80]; (**e**) tetrac/^{64}Cu-DOTA-liposome (*left*) and ^{64}Cu-DOTA-liposome (*right*) [85]; (**f**) Mannose liposomes for remote loading of the ^{64}Cu-DOTA [84]; (**g**) Loading of $^{64}Cu^{2+}$ into liposomes [82]; (**h**) PEGylated (DSPE-PEG2000) targeted TATE-liposome [83]

7 Additional Types of PET Nanoparticle Agents

7.1 Carbon Nanotubes (CNTs)

Carbon nanotubes are allotropes of carbon having a cylindrical structure. CNTs have interesting properties for use in a diverse array of materials, owing to their extraordinary thermal conductivity, mechanical, and electrical properties. CNTs are categorized as single walled (SWNT) and multiwalled (MWNT) [87]. SWNTs consist of a one-atom thick layer of graphene, whereas MWNTs consist of multiple rolled layers of graphene. The normal organ biodistribution and pharmacokinetics of ^{86}Y-labeled SWNTs were investigated in non-tumor-bearing athymic nude mice

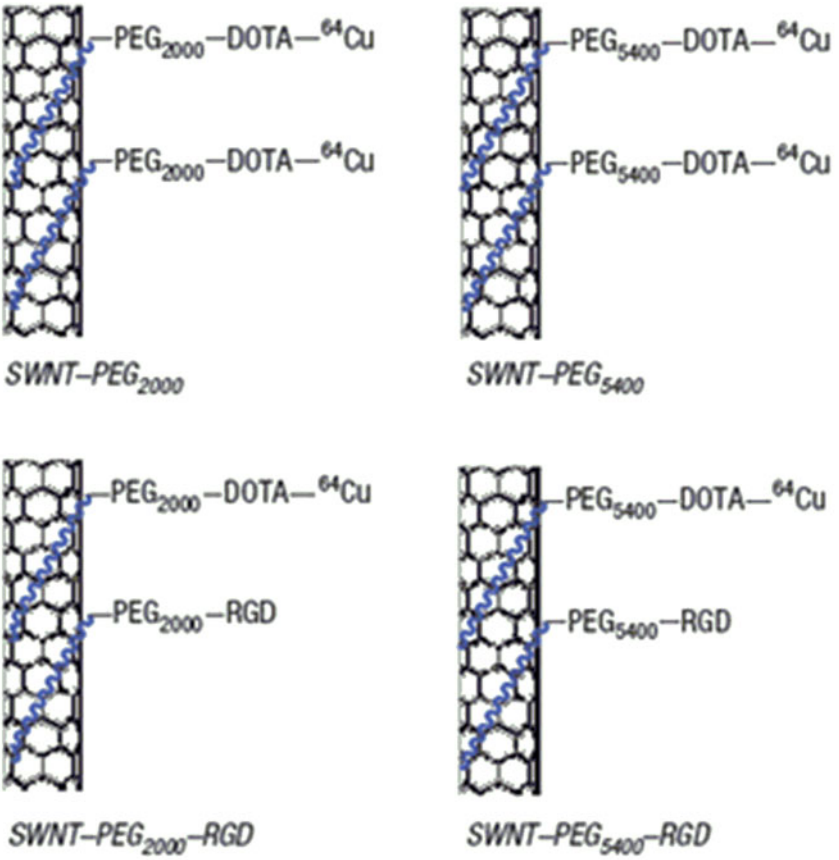

Fig. 12 Schematic drawing of noncovalently functionalized SWNTs with PEG2000 and PEG5400 with ^{64}Cu, either with or without RGD peptides for targeting integrin $\alpha_4\beta_1$ [50]

to determine the clearance patterns, which indicated blood clearance within 3 h and distribution predominantly to the kidneys, liver, spleen, and bone [88]. RGD-conjugated (targeting integrin $\alpha_v\beta_3$) and nontargeted SWNTs (diameter: 1–5 nm; length: 100–300 nm) with varying lengths of PEG chains were labeled with Cu-64 and investigated in U87MG human glioma tumor-bearing mice (Fig. 12) [50]. The authors showed that PEG_{5400} extended the circulation time of the nanoparticles, and RGD peptides improved tumor uptake compared to nontargeted agents. Although for PET imaging studies there was no observable toxicity of the radiolabeled SWNTs [50], the carbon nanotube class of nanoparticle has fallen out of favor due to health and safety issues [56].

7.2 Micelle-Based Nanoparticles

Micelle-based nanoparticles have hydrophilic regions that are in contact with the surrounding solvent, typically aqueous media, with hydrophobic regions in the center of the micelle that can sequester lipophilic drugs or other cargo. Micelles can be aggregates of small surfactant molecules (MW in the hundreds), or aggregates of larger amphiphilic block copolymers (MW in the thousands or tens of thousands).

Diblock co-polymer shell cross-linked nanoparticles (SCK-NPs) have been incorporated with DOTA (Fig. 13a) [89] and TETA [90] chelators for labeling with Cu-64. In one of the first studies of ^{64}Cu-labeled SCK-NPs (PEG_{1600} spacer; ~20 nm), Cu-64 was labeled using the TETA chelator to nontargeted and folate-targeted nanoparticles, and biodistribution was determined in folate-receptor positive KB tumor-bearing mice [90]. Targeted and nontargeted agents cleared through the liver, lung, and spleen, and there was no significant difference in tumor uptake. Zeng et al. achieved very high specific activity by incorporation of azide groups in the core of the nanoparticles, followed by reaction of ^{64}Cu-DOTA conjugated to the strained alkyne, dibenzylcyclooctyne (DBCO) under copper-free click chemistry conditions. They achieved 975 Ci/μmol, amplifying the amount of ^{64}Cu-labeling by a factor of 500 compared to direct labeling of chelator-SCK-NPs [89].

To address the question of whether incorporation of a more stable Cu(II) chelator positively impacts U87MG tumor uptake and nontarget tissue biodistribution of ^{64}Cu-labeled tri-block polymeric micelles (Fig. 13b) [3], DOTA was compared to CB-TE2A, which forms highly stable Cu(II) complexes in vivo [2, 91]. The ^{64}Cu-labeled CB-TE2A micelles showed somewhat slower blood clearance leading to higher tumor uptake. However, the tumor:blood ratios of the DOTA vs. CB-TE2A micelles were not significantly different. Nontarget tissue uptake of the two ^{64}Cu-labeled micelles was similar. The authors concluded that although DOTA is not an ideal ^{64}Cu-chelator for smaller molecules, it is adequate for labeling micellular nanoparticles.

Amphiphilic graft copolymers and associated comb nanoparticles (CNPs) were designed to be tunable with respect to their composition and to be modified with a controlled number of RGD peptide moieties (Fig. 13c) [92]. The 20–23 nm CNPs consisted of four building blocks: a) PEG units; b) a hydrophobic methyl mathacrylate backbone; c) DOTA chelator for Cu-64 labeling; and d) GRGDS linear integrin $\alpha_v\beta_3$ targeting peptides. The 20 % RGD CNPs demonstrated highest affinity for integrin $\alpha_v\beta_3$ in an in vitro assay, and the ^{64}Cu-labeled 20 % RGD CNPs showed the highest cell associated activity in cultured U87MG cells. A similar strategy was used to produce DOTA-CNPs modified with C-type natriuretic factor binding peptide (CANF), which binds to the cell surface natriuretic peptide clearance receptor (NPRC) [93]. The authors investigated imaging of prostate cancer in human CWR 22 tumor-bearing mice with ^{64}Cu-DOTA-CANF-CNPs, and found specific uptake in the tumor; however, histologically, it was shown that staining for NPRC is found in pools of inflammatory cells in the tumor, and not in the tumor itself. Targeting NPRC through the CANF-CNPs

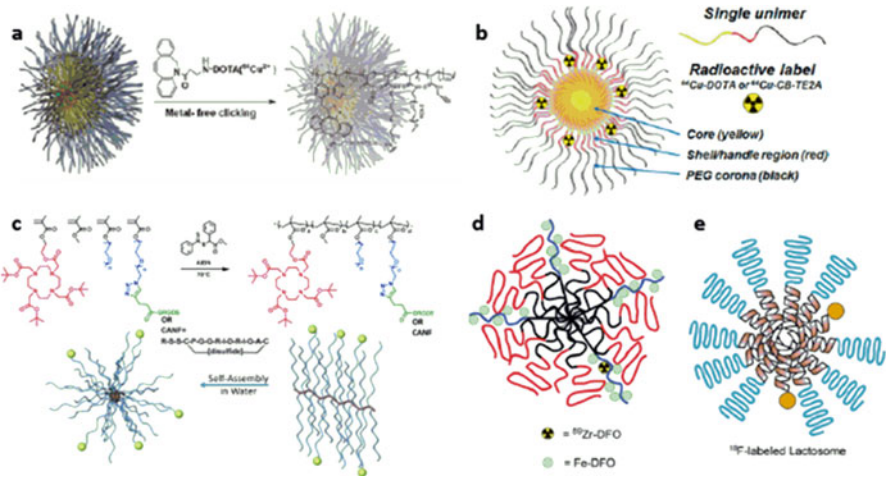

Fig. 13 Micelle-based nanoparticles for PET imaging. (**a**) strategy for metal-free click chemistry to label SCK-NPs with Cu-64, resulting in exceptionally high specific activity [89]; (**b**) tri-block polymeric micelles that are conjugated with the chelators DOTA or CB-TE2A for Cu-64 labeling [3]; (**c**) amphiphilic graft copolymers and associated comb nanoparticles (CNPs) that are tunable for adding the DOTA chelator and targeting peptides GRGDS or the CANF peptide [92, 93]; (**d**) amphiphilic diblock copolymer micelle that contains Fe-DFO for MRI and ^{89}Zr for PET [94]; (**e**) ^{18}F-labeled amphiphilic depsipeptide (Lactosome) composed of poly(L-lactic acid)-*block*-poly(sarcosine) [95]

may provide an interesting means of imaging and therapy of inflammatory cell types, although the specific cells targeted were not enumerated.

An amphiphilic diblock copolymer micelle was designed to incorporate Zr-89 and Fe(III) for PET and T_1-weighted MRI, through chelation of the two metals with deferoxamine (DFO) (Fig. 13d) [94]. The micelles were formed by self-assembly of a mixture of polybutadiene-b-polyethyleneoxide (PBD-b-PEO) and polybutadiene-b-polyacrylicacid (PBD-b-PAA) polymers, with the acetic acid residues functionalized with ^{89}Zr-DFO for PET and Fe-DFO for MRI. The dual PET/MRI-capable nontargeted particles were investigated in LS174R human colorectal tumor-bearing mice. Biodistribution based on gamma counting of Zr-89 showed high liver and spleen uptake (30–40 % ID/g), with tumor uptake being modest (4–6 % ID/g). Contrast of the subcutaneous tumors was observed with both imaging modalities, however.

Fluorine-18 has been labeled to an amphiphilic polydepsipeptide ("Lactosome") composed of poly(L-lactic acid)-*block*-poly(sarcosine) (Fig. 13e) [95], and was investigated for biodistribution and PET imaging in Hela-tumor-bearing mice. Due to the short half-life of F-18 ($T_{1/2}$ = 110 min), the time limit for imaging was 6 h, and the blood activity remained high (25 % ID/g) with low tumor uptake (<5 % ID/g).

7.3 Nanogels

Almutairi and colleagues developed chelator crosslinking hydrogel nanoparticles (nanogels) that have applications for MRI and PET imaging. The initial nanogels were polyacrylamide (PAA)-based and incorporated acyclic (DTPA) and cyclic (DOTA) chelators for Gd^{3+} [96]. The DOTA macrocycle was *C*-substituted to allow coordination of all carboxylate moieties to the Gd^{3+}. These nontargeted PAA nanogels were then modified by incorporating NOTA chelators for labeling with Cu-64 for PET imaging, with comparison to the ^{64}Cu-DOTA-nanogels (Fig. 14a) [97]. In 4T1 mouse mammary tumor-bearing mice, the ^{64}Cu-NOTA-nanogels showed surprisingly low liver and spleen accumulation compared to the DOTA agent (~5–15 % vs. 15–20 % ID/g) with tumor:liver ratios >1 (Fig. 14b). Tumor uptake for the NOTA-nanogels increased to >15 % ID/g in subcutaneous 4T1 tumors at 48 h postinjection, and as high as 30 % ID/g in small tumor metastases, which is also much higher than reported for other ^{64}Cu-labeled nanoparticles in various tumor models [39, 93, 98, 99].

7.4 Porphysomes

^{64}Cu-porphysomes are self-assembled from a single porphyrin-lipid building block, and similar to the chelator-cross-linked nanogels by the Almutairi lab [97], they do not require conjugation of chelators to the nanoparticle itself (Fig. 15) [100]. Another advantage of the porphysome platform is that it is intrinsically fluorescent, allowing for optical imaging in the same study as PET imaging. The uptake of ^{64}Cu-porphysomes in orthotopic prostate tumors (PC3 and 22RV1) was relatively low (5–7 % ID/g) at 24 h postinjection, while liver was 15–20 % ID/g and spleen uptake was >100 % ID/g. Encouragingly, small prostate tumor bone metastases in the lower extremities were readily imaged with ^{64}Cu-porphysomes.

7.5 Zinc Oxide Nanoparticles

Zinc oxide nanoparticles (ZONs) have many applications and have been used as sensors, in electronics, cosmetics, food additives, and the medical industry [101, 102] and are attractive due to their low toxicity and biodegradability [103]. ZONs of varying sizes (20 and 100 nm) have been labeled with F-18 by click chemistry to trace their biodistribution after oral administration [104]. Based on the lack of bone uptake, it was surmised there was minimal defluorination, with the majority of ^{18}F-activity observed in the gut.

Hong et al. investigated ^{64}Cu-labeled ZONs (~80–100 nm) that were either nontargeted or conjugated to the TRC105 antibody against CD105, which is found

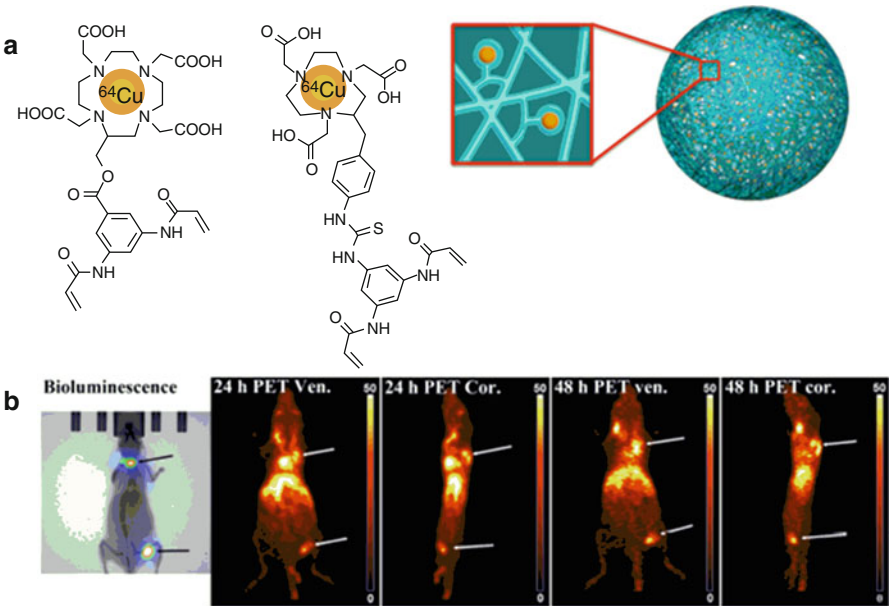

Fig. 14 (**a**) Schematic of ^{64}Cu-labeled DOTA and NOTA chelator cross-linked nanogels. (**b**) Bioluminescence and ^{64}Cu-NOTA-nanogel PET images of mice with 4 T1 tumors in their shoulder bone and lymph node in the hind leg. Uptake of ^{64}Cu-NOTA-nanogel in the metastases reached 20–30 % ID/g at 48 h postinjection [97]

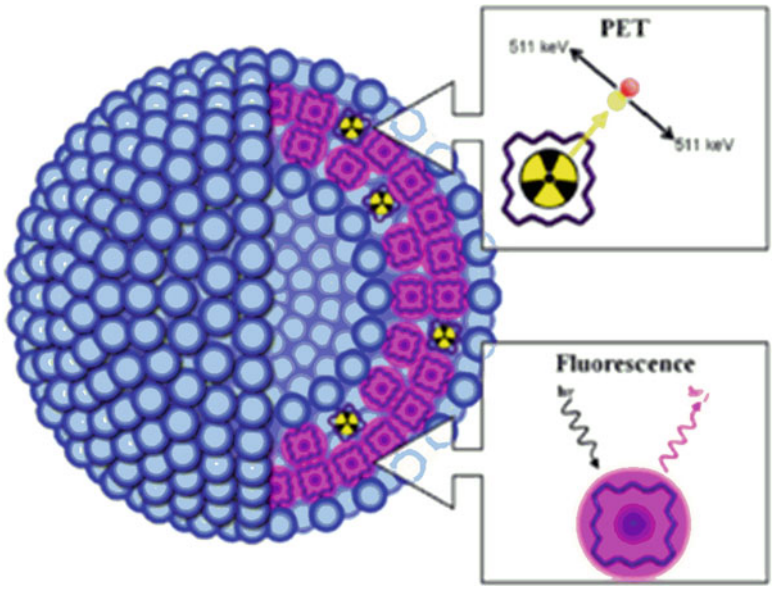

Fig. 15 Schematic diagram showing PET and fluorescence imaging properties of porphysome nanoparticles [101]

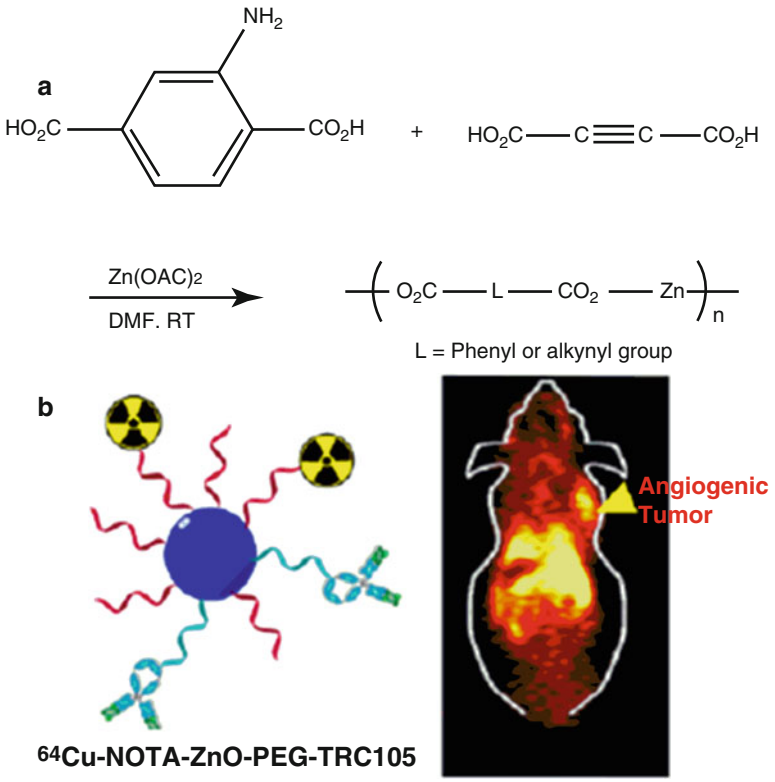

Fig. 16 (**a**) Preparation of coordination polymer precursor [107]; (**b**) red fluorescent ZnO nanoparticle conjugated with TRC105 for imaging CD105 as a marker of tumor vasculature. The nanoparticle is labeled with Cu-64 for PET imaging in 4T1 tumor-bearing mice [106]

on endothelial cells for imaging angiogenesis [105]. The ZONs used in this study incorporated a coordination polymer precursor consisting of a carboxylic acid functionalized organic molecule (Fig. 16a), and the particles were prepared by calcination at high temperatures (e.g., 550 °C) of the coordination polymers as described [106]. The authors found that the ^{64}Cu-NOTA-ZON-PEG-TRC105 particles were taken up in 4T1 tumors in significantly higher amounts than the nontargeted ZONs (~4–6 % ID/g vs. ~2–3 %ID/g) (Fig. 16b). Liver uptake was 15–20 % ID/g, and spleen was ~10 % ID/g. Overall, the tumor:non-tumor ratios were modest, even for the targeted particles.

8 Conclusions

There have been significant advances over the past decade in the development of radiolabeled nanoparticles for PET imaging of cancer. The advantages of PET, which include the ability to visualize disease with nano- to picomolar concentrations of tracer, are well suited toward nanoparticles as diagnostic or theranostic agents. The plethora of classes of nanoparticles that have been investigated is encouraging, and although there are currently few agents that have moved on to human studies, it is anticipated that many more agents will advance in this direction over the next 5 years. The jury is still out regarding whether targeted or nontargeted nanoparticles are best suited for tumor imaging; however, the answer to this question is most likely that both will ultimately be used clinically, and it will be highly dependent on the type of nanostructure.

References

1. Cook G. Oncological molecular imaging: nuclear medicine techniques. Br J Radiol. 2014.
2. Boswell CA, Sun X, Niu W, Weisman GR, Wong EH, Rheingold AL, et al. Comparative in vivo stability of copper-64-labeled cross-bridged and conventional tetraazamacrocyclic complexes. J Med Chem. 2004;47(6):1465–74.
3. Jensen AI, Binderup T, Kumar EP, Kjaer A, Rasmussen PH, Andresen TL. Positron emission tomography based analysis of long-circulating cross-linked triblock polymeric micelles in a U87MG mouse xenograft model and comparison of DOTA and CB-TE2A as chelators of copper-64. Biomacromolecules. 2014;15(5):1625–33. doi:10.1021/bm401871w.
4. Deri MA, Ponnala S, Zeglis BM, Pohl G, Dannenberg JJ, Lewis JS, et al. Alternative chelator for (8)(9)Zr radiopharmaceuticals: radiolabeling and evaluation of 3,4,3-(LI-1,2-HOPO). J Med Chem. 2014;57(11):4849–60. doi:10.1021/jm500389b.
5. Pandya DN, Pailloux S, Tatum D, Magda D, Wadas TJ. Di-macrocyclic terephthalamide ligands as chelators for the PET radionuclide zirconium-89. Chem Commun (Camb). 2015;51(12):2301–3. doi:10.1039/c4cc09256b.
6. Lee JE, Lee N, Kim T, Kim J, Hyeon T. Multifunctional mesoporous silica nanocomposite nanoparticles for theranostic applications. Acc Chem Res. 2011;44(10):893–902. doi:10.1021/ar2000259.
7. Rosenholm JM, Mamaeva V, Sahlgren C, Linden M. Nanoparticles in targeted cancer therapy: mesoporous silica nanoparticles entering preclinical development stage. Nanomedicine (Lond). 2012;7(1):111–20. doi:10.2217/nnm.11.166.
8. Meng H, Xue M, Xia T, Ji Z, Tarn DY, Zink JI, et al. Use of size and a copolymer design feature to improve the biodistribution and the enhanced permeability and retention effect of doxorubicin-loaded mesoporous silica nanoparticles in a murine xenograft tumor model. ACS Nano. 2011;5(5):4131–44. doi:10.1021/nn200809t.
9. Pan L, He Q, Liu J, Chen Y, Ma M, Zhang L, et al. Nuclear-targeted drug delivery of TAT peptide-conjugated monodisperse mesoporous silica nanoparticles. J Am Chem Soc. 2012;134(13):5722–5. doi:10.1021/ja211035w.
10. Caltagirone C, Bettoschi A, Garau A, Montis R. Silica-based nanoparticles: a versatile tool for the development of efficient imaging agents. Chem Soc Rev. 2015;44(14):4645–71. doi:10.1039/c4cs00270a.
11. Taylor KM, Kim JS, Rieter WJ, An H, Lin W, Lin W. Mesoporous silica nanospheres as highly efficient MRI contrast agents. J Am Chem Soc. 2008;130(7):2154–5. doi:10.1021/ja710193c.

12. Lu J, Liong M, Li Z, Zink JI, Tamanoi F. Biocompatibility, biodistribution, and drug-delivery efficiency of mesoporous silica nanoparticles for cancer therapy in animals. Small. 2010;6(16):1794–805. doi:10.1002/smll.201000538.
13. Lee SB, Kim HL, Jeong HJ, Lim ST, Sohn MH, Kim DW. Mesoporous silica nanoparticle pretargeting for PET imaging based on a rapid bioorthogonal reaction in a living body. Angew Chem Int Ed Engl. 2013;52(40):10549–52. doi:10.1002/anie.201304026.
14. Kim DW. Bioorthogonal click chemistry for fluorine-18 labeling protocols under physiological friendreactioncondition.JFluorChem.2015;174:142–7.doi:10.1016/j.jfluchem.2014.11.009.
15. Miller L, Winter G, Baur B, Witulla B, Solbach C, Reske S, et al. Synthesis, characterization, and biodistribution of multiple 89Zr-labeled pore-expanded mesoporous silica nanoparticles for PET. Nanoscale. 2014;6(9):4928–35. doi:10.1039/c3nr06800e.
16. Chen F, Nayak TR, Goel S, Valdovinos HF, Hong H, Theuer CP, et al. In vivo tumor vasculature targeted PET/NIRF imaging with TRC105(Fab)-conjugated, dual-labeled mesoporous silica nanoparticles. Mol Pharm. 2014;11(11):4007–14. doi:10.1021/mp500306k.
17. Kang WJ, Lee J, Lee YS, Cho S, Ali BA, Al-Khedhairy AA, et al. Multimodal imaging probe for targeting cancer cells using uMUC-1 aptamer. Colloids Surf B Biointerfaces. 2015;136:134–40. doi:10.1016/j.colsurfb.2015.09.004.
18. Chakravarty R, Goel S, Hong H, Chen F, Valdovinos HF, Hernandez R, et al. Hollow mesoporous silica nanoparticles for tumor vasculature targeting and PET image-guided drug delivery. Nanomedicine (Lond). 2015;10(8):1233–46. doi:10.2217/nnm.14.226.
19. Cobley CM, Chen J, Cho EC, Wang LV, Xia Y. Gold nanostructures: a class of multifunctional materials for biomedical applications. Chem Soc Rev. 2011;40(1):44–56. doi:10.1039/b821763g.
20. Sperling RA, Gil PR, Zhang F, Zanella M, Parak WJ. Biological applications of gold nanoparticles. Chem Soc Rev. 2008;37(9):1896–908. doi:10.1039/b712170a.
21. Daniel MC, Astruc D. Gold nanoparticles: assembly, supramolecular chemistry, quantum-size-related properties, and applications toward biology, catalysis, and nanotechnology. Chem Rev. 2004;104(1):293–346. doi:10.1021/cr030698+.
22. Chen J, Glaus C, Laforest R, Zhang Q, Yang M, Gidding M, et al. Gold nanocages as photothermal transducers for cancer treatment. Small. 2010;6(7):811–7. doi:10.1002/smll.200902216.
23. Liu Y, Yuan H, Kersey FR, Register JK, Parrott MC, Vo-Dinh T. Plasmonic gold nanostars for multi-modality sensing and diagnostics. Sensors. 2015;15(2):3706–20. doi:10.3390/s150203706.
24. Vo-Dinh T, Liu Y, Fales AM, Ngo H, Wang HN, Register JK, et al. SERS nanosensors and nanoreporters: golden opportunities in biomedical applications. Wiley Interdiscip Rev Nanomed Nanobiotechnol. 2015;7(1):17–33. doi:10.1002/wnan.1283.
25. Khlebtsov N, Bogatyrev V, Dykman L, Khlebtsov B, Staroverov S, Shirokov A, et al. Analytical and theranostic applications of gold nanoparticles and multifunctional nanocomposites. Theranostics. 2013;3(3):167–80. doi:10.7150/thno.5716.
26. Brust M, Fink J, Bethell D, Schiffrin D, Kiely C. Synthesis and reactions of functionalised gold nanoparticles. J Chem Soc Chem Commun. 1995;16:1655–6.
27. Leff DV, Brandt L, Heath JR. Synthesis and characterization of hydrophobic, organically-soluble gold nanocrystals functionalized with primary amines. Langmuir. 1996;12(20):4723–30.
28. Anshup A, Venkataraman JS, Subramaniam C, Kumar RR, Priya S, Kumar TS, et al. Growth of gold nanoparticles in human cells. Langmuir. 2005;21(25):11562–7.
29. Huang X, El-Sayed IH, Qian W, El-Sayed MA. Cancer cell imaging and photothermal therapy in the near-infrared region by using gold nanorods. J Am Chem Soc. 2006;128(6):2115–20.
30. Caruso F, Spasova M, Salgueiriño-Maceira V, Liz-Marzán L. Multilayer assemblies of silica-encapsulated gold nanoparticles on decomposable colloid templates. Adv Mater. 2001;13(14):1090–4.
31. Oldenburg SJ, Jackson JB, Westcott SL, Halas N. Infrared extinction properties of gold nanoshells. Appl Phys Lett. 1999;75(19):2897–9.
32. Chen J, McLellan JM, Siekkinen A, Xiong Y, Li Z-Y, Xia Y. Facile synthesis of gold-silver nanocages with controllable pores on the surface. J Am Chem Soc. 2006;128(46):14776–7.

33. Chen J, Saeki F, Wiley BJ, Cang H, Cobb MJ, Li Z-Y, et al. Gold nanocages: bioconjugation and their potential use as optical imaging contrast agents. Nano Lett. 2005;5(3):473–7.
34. Giersig M, Mulvaney P. Preparation of ordered colloid monolayers by electrophoretic deposition. Langmuir. 1993;9(12):3408–13.
35. Pirollo KF, Chang EH. Does a targeting ligand influence nanoparticle tumor localization or uptake? Trends Biotechnol. 2008;26(10):552–8. http://dx.doi.org/10.1016/j.tibtech.2008.06.007.
36. Xie H, Diagaradjane P, Deorukhkar AA, Goins B, Bao A, Phillips WT, et al. Integrin α(v) β(3)-targeted gold nanoshells augment tumor vasculature-specific imaging and therapy. Int J Nanomedicine. 2011;6:259–69. doi:10.2147/ijn.s15479.
37. Zhou M, Zhang R, Huang M, Lu W, Song S, Melancon MP, et al. A chelator-free multifunctional [64Cu] CuS nanoparticle platform for simultaneous micro-PET/CT imaging and photothermal ablation therapy. J Am Chem Soc. 2010;132(43):15351–8.
38. Zhao Y, Sultan D, Detering L, Cho S, Sun G, Pierce R, et al. Copper-64-alloyed gold nanoparticles for cancer imaging: improved radiolabel stability and diagnostic accuracy. Angew Chem Int Ed. 2014;53(1):156–9.
39. Zhao Y, Sultan D, Detering L, Luehmann H, Liu Y. Facile synthesis, pharmacokinetic and systemic clearance evaluation, and positron emission tomography cancer imaging of 64Cu-Au alloy nanoclusters. Nanoscale. 2014;6(22):13501–9. doi:10.1039/c4nr04569f.
40. Tian M, Lu W, Zhang R, Xiong C, Ensor J, Nazario J, et al. Tumor uptake of hollow gold nanospheres after intravenous and intra-arterial injection: PET/CT study in a rabbit VX2 liver cancer model. Mol Imaging Biol. 2013;15(5):614–24. doi:10.1007/s11307-013-0635-x.
41. Tsoukalas C, Laurent G, Sánchez GJ, Tsotakos T, Bazzi R, Stellas D, et al. Initial in vitro and in vivo assessment of Au@ DTDTPA-RGD nanoparticles for Gd-MRI and 68Ga-PET dual modality imaging. EJNMMI Phys. 2015;2 Suppl 1:A89.
42. Karmani L, Bouchat V, Bouzin C, Levêque P, Labar D, Bol A, et al. 89Zr-labeled anti-endoglin antibody-targeted gold nanoparticles for imaging cancer: implications for future cancer therapy. Nanomedicine. 2014;9(13):1923–37.
43. Choi CH, Zuckerman JE, Webster P, Davis ME. Targeting kidney mesangium by nanoparticles of defined size. Proc Natl Acad Sci U S A. 2011;108(16):6656–61. doi:10.1073/pnas.1103573108.
44. Burns AA, Vider J, Ow H, Herz E, Penate-Medina O, Baumgart M, et al. Fluorescent silica nanoparticles with efficient urinary excretion for nanomedicine. Nano Lett. 2009;9(1):442–8. doi:10.1021/nl803405h.
45. Longmire M, Choyke PL, Kobayashi H. Clearance properties of nano-sized particles and molecules as imaging agents: considerations and caveats. Nanomedicine. 2008;3(5):703–17. doi:10.2217/17435889.3.5.703.
46. Kharissova OV, Kharisov BI, Jiménez-Pérez VM, Flores BM, Méndez UO. Ultrasmall particles and nanocomposites: state of the art. RSC Adv. 2013;3(45):22648–82.
47. Schipper ML, Iyer G, Koh AL, Cheng Z, Ebenstein Y, Aharoni A, et al. Particle size, surface coating, and PEGylation influence the biodistribution of quantum dots in living mice. Small. 2009;5(1):126–34. doi:10.1002/smll.200800003.
48. Jokerst JV, Lobovkina T, Zare RN, Gambhir SS. Nanoparticle PEGylation for imaging and therapy. Nanomedicine. 2011;6(4):715–28. doi:10.2217/nnm.11.19.
49. You J, Zhou J, Zhou M, Liu Y, Robertson JD, Liang D, et al. Pharmacokinetics, clearance, and biosafety of polyethylene glycol-coated hollow gold nanospheres. Part Fibre Toxicol. 2014;11(1):1–14.
50. Liu Z, Cai W, He L, Nakayama N, Chen K, Sun X, et al. In vivo biodistribution and highly efficient tumour targeting of carbon nanotubes in mice. Nat Nanotechnol. 2007;2(1):47–52. doi:10.1038/nnano.2006.170.
51. Cui L, Lin Q, Jin CS, Jiang W, Huang H, Ding L, et al. A PEGylation-free biomimetic porphyrin nanoplatform for personalized cancer theranostics. ACS Nano. 2015;9(4):4484–95. doi:10.1021/acsnano.5b01077.
52. Pombo-García K, Zarschler K, Barreto JA, Hesse J, Spiccia L, Graham B, et al. Design, synthesis, characterisation and in vitro studies of hydrophilic, colloidally stable, 64Cu(ii)-

labelled, ultra-small iron oxide nanoparticles in a range of human cell lines. RSC Adv. 2013;3(44):22443. doi:10.1039/c3ra43726d.
53. Zhou M, Li J, Liang S, Sood AK, Liang D, Li C. CuS nanodots with ultrahigh efficient renal clearance for positron emission tomography imaging and image-guided photothermal therapy. ACS Nano. 2015;9(7):7085–96. doi:10.1021/acsnano.5b02635.
54. Benezra M, Penate-Medina O, Zanzonico PB, Schaer D, Ow H, Burns A, et al. Multimodal silica nanoparticles are effective cancer-targeted probes in a model of human melanoma. J Clin Invest. 2011;121(7):2768–80. doi:10.1172/JCI45600.
55. Phillips E, Penate-Medina O, Zanzonico PB, Carvajal RD, Mohan P, Ye Y, et al. Clinical translation of an ultrasmall inorganic optical-PET imaging nanoparticle probe. Sci Transl Med. 2014;6(260):260ra149. doi:10.1126/scitranslmed.3009524.
56. Liu Y, Zhao Y, Sun B, Chen C. Understanding the toxicity of carbon nanotubes. Acc Chem Res. 2013;46(3):702–13. doi:10.1021/ar300028m.
57. Gao F, Cai P, Yang W, Xue J, Gao L, Liu R, et al. Ultrasmall [(64)Cu]Cu nanoclusters for targeting orthotopic lung tumors using accurate positron emission tomography imaging. ACS Nano. 2015;9(5):4976–86. doi:10.1021/nn507130k.
58. Truillet C, Bouziotis P, Tsoukalas C, Brugiere J, Martini M, Sancey L, et al. Ultrasmall particles for Gd-MRI and (68) Ga-PET dual imaging. Contrast Media Mol Imaging. 2015;10(4):309–19. doi:10.1002/cmmi.1633.
59. Yang BY, Moon S-H, Seelam SR, Jeon MJ, Lee Y-S, Lee DS, et al. Development of a multimodal imaging probe by encapsulating iron oxide nanoparticles with functionalized amphiphiles for lymph node imaging. Nanomedicine. 2015;10(12):1899–910.
60. Lee S, Chen X. Dual-modality probes for in vivo molecular imaging. Mol Imaging. 2009;8(2):87.
61. Lee JH, Sherlock SP, Terashima M, Kosuge H, Suzuki Y, Goodwin A, et al. High-contrast in vivo visualization of microvessels using novel FeCo/GC magnetic nanocrystals. Magn Reson Med. 2009;62(6):1497–509.
62. Yang H, Zhang C, Shi X, Hu H, Du X, Fang Y, et al. Water-soluble superparamagnetic manganese ferrite nanoparticles for magnetic resonance imaging. Biomaterials. 2010;31(13):3667–73.
63. Tromsdorf UI, Bigall NC, Kaul MG, Bruns OT, Nikolic MS, Mollwitz B, et al. Size and surface effects on the MRI relaxivity of manganese ferrite nanoparticle contrast agents. Nano Lett. 2007;7(8):2422–7.
64. Xie J, Chen K, Huang J, Lee S, Wang J, Gao J, et al. PET/NIRF/MRI triple functional iron oxide nanoparticles. Biomaterials. 2010;31(11):3016–22.
65. Lee H-Y, Li Z, Chen K, Hsu AR, Xu C, Xie J, et al. PET/MRI dual-modality tumor imaging using arginine-glycine-aspartic (RGD)-conjugated radiolabeled iron oxide nanoparticles. J Nucl Med. 2008;49(8):1371–9.
66. Groult H, Ruiz-Cabello J, Pellico J, Lechuga-Vieco AV, Bhavesh R, Zamai M, et al. Parallel multifunctionalization of nanoparticles: a one-step modular approach for in vivo imaging. Bioconjug Chem. 2014;26(1):153–60.
67. Yang M, Cheng K, Qi S, Liu H, Jiang Y, Jiang H, et al. Affibody modified and radiolabeled gold–iron oxide hetero-nanostructures for tumor PET, optical and MR imaging. Biomaterials. 2013;34(11):2796–806.
68. Caride VJ. Liposomes as carriers of imaging agents. Crit Rev Ther Drug Carrier Syst. 1985;1(2):121–53.
69. Tilcock C, Ahkong QF, Fisher D. Polymer-derivatized technetium 99mTc-labeled liposomal blood pool agents for nuclear medicine applications. Biochim Biophys Acta Biomembr. 1993;1148(1):77–84.
70. Krause W, Klopp R, Leike J, Sachse A, Schuhmann-Giampieri G. Liposomes in diagnostic imaging-comparison of modalities-in-vivo visualization of liposomes. J Liposome Res. 1995;5(1):1–26.

71. Tilcock C, Philippot J, Schuber F. Imaging tools: liposomal agents for nuclear medicine, computed tomography, magnetic resonance, and ultrasound. Liposomes as tools in basic research and industry. 1995. p. 225–40.
72. Tilcock C. Delivery of contrast agents for magnetic resonance imaging, computed tomography, nuclear medicine and ultrasound. Adv Drug Deliv Rev. 1999;37(1):33–51.
73. Phillips WT, Goins BA, Bao A. Radioactive liposomes. Wiley Interdiscip Rev Nanomed Nanobiotechnol. 2009;1(1):69–83.
74. Jensen AT, Binderup T, Andresen TL, Kjaer A, Rasmussen PH. PET imaging of liposomes labeled with an [(1)(8)F]-fluorocholesteryl ether probe prepared by automated radiosynthesis. J Liposome Res. 2012;22(4):295–305. doi:10.3109/08982104.2012.698418.
75. Emmetiere F, Irwin C, Viola-Villegas NT, Longo V, Cheal SM, Zanzonico P, et al. (18) F-labeled-bioorthogonal liposomes for in vivo targeting. Bioconjug Chem. 2013;24(11):1784–9. doi:10.1021/bc400322h.
76. Perk LR, Visser GW, Vosjan MJ, Stigter-van Walsum M, Tijink BM, Leemans CR, et al. (89) Zr as a PET surrogate radioisotope for scouting biodistribution of the therapeutic radiometals (90)Y and (177)Lu in tumor-bearing nude mice after coupling to the internalizing antibody cetuximab. J Nucl Med. 2005;46(11):1898–906.
77. Lubberink M, Herzog H. Quantitative imaging of 124I and 86Y with PET. Eur J Nucl Med Mol Imaging. 2011;38 Suppl 1:S10–8. doi:10.1007/s00259-011-1768-2.
78. Perez-Medina C, Abdel-Atti D, Zhang Y, Longo VA, Irwin CP, Binderup T, et al. A modular labeling strategy for in vivo PET and near-infrared fluorescence imaging of nanoparticle tumor targeting. J Nucl Med. 2014;55(10):1706–11. doi:10.2967/jnumed.114.141861.
79. Seo JW, Mahakian LM, Tam S, Qin S, Ingham ES, Meares CF, et al. The pharmacokinetics of Zr-89 labeled liposomes over extended periods in a murine tumor model. Nucl Med Biol. 2015;42(2):155–63. doi:10.1016/j.nucmedbio.2014.09.001.
80. Abou DS, Thorek DL, Ramos NN, Pinkse MW, Wolterbeek HT, Carlin SD, et al. (89) Zr-labeled paramagnetic octreotide-liposomes for PET-MR imaging of cancer. Pharm Res. 2013;30(3):878–88. doi:10.1007/s11095-012-0929-8.
81. Petersen AL, Binderup T, Rasmussen P, Henriksen JR, Elema DR, Kjaer A, et al. 64Cu loaded liposomes as positron emission tomography imaging agents. Biomaterials. 2011;32(9):2334–41. doi:10.1016/j.biomaterials.2010.11.059.
82. Henriksen JR, Petersen AL, Hansen AE, Frankaer CG, Harris P, Elema DR, et al. Remote loading of (64)Cu(2+) into liposomes without the use of ion transport enhancers. ACS Appl Mater Interfaces. 2015;7(41):22796–806. doi:10.1021/acsami.5b04612.
83. Petersen AL, Binderup T, Jolck RI, Rasmussen P, Henriksen JR, Pfeifer AK, et al. Positron emission tomography evaluation of somatostatin receptor targeted 64Cu-TATE-liposomes in a human neuroendocrine carcinoma mouse model. J Contr Release. 2012;160(2):254–63. doi:10.1016/j.jconrel.2011.12.038.
84. Locke LW, Mayo MW, Yoo AD, Williams MB, Berr SS. PET imaging of tumor associated macrophages using mannose coated 64Cu liposomes. Biomaterials. 2012;33(31):7785–93. doi:10.1016/j.biomaterials.2012.07.022.
85. Kang CM, Koo HJ, Lee S, Lee KC, Oh YK, Choe YS. 64Cu-labeled tetraiodothyroacetic acid-conjugated liposomes for PET imaging of tumor angiogenesis. Nucl Med Biol. 2013;40(8):1018–24. doi:10.1016/j.nucmedbio.2013.08.003.
86. Wong AW, Ormsby E, Zhang H, Seo JW, Mahakian LM, Caskey CF, et al. A comparison of image contrast with (64)Cu-labeled long circulating liposomes and (18)F-FDG in a murine model of mammary carcinoma. Am J Nucl Med Mol Imaging. 2013;3(1):32–43.
87. Gong H, Peng R, Liu Z. Carbon nanotubes for biomedical imaging: the recent advances. Adv Drug Deliv Rev. 2013;65(15):1951–63. doi:10.1016/j.addr.2013.10.002.
88. McDevitt MR, Chattopadhyay D, Jaggi JS, Finn RD, Zanzonico PB, Villa C et al. PET imaging of soluble yttrium-86-labeled carbon nanotubes in mice. PLoS One. 2007;2(9):e907. 10.1371/journal.pone.0000907.
89. Zeng D, Lee NS, Liu Y, Zhou D, Dence CS, Wooley KL, et al. 64Cu Core-labeled nanoparticles with high specific activity via metal-free click chemistry. ACS Nano. 2012;6(6):5209–19. doi:10.1021/nn300974s.

90. Rossin R, Pan D, Qi K, Turner JL, Sun X, Wooley KL, et al. 64Cu-labeled folate-conjugated shell cross-linked nanoparticles for tumor imaging and radiotherapy: synthesis, radiolabeling, and biologic evaluation. J Nucl Med. 2005;46(7):1210–8.
91. Sun X, Wuest M, Weisman GR, Wong EH, Reed DP, Boswell CA, et al. Radiolabeling and in vivo behavior of copper-64-labeled cross-bridged cyclam ligands. J Med Chem. 2002;45:469–77.
92. Shokeen M, Pressly ED, Hagooly A, Zheleznyak A, Ramos N, Fiamengo AL, et al. Evaluation of multivalent, functional polymeric nanoparticles for imaging applications. ACS Nano. 2011;5(2):738–47. doi:10.1021/nn102278w.
93. Pressly ED, Pierce RA, Connal LA, Hawker CJ, Liu Y. Nanoparticle PET/CT imaging of natriuretic peptide clearance receptor in prostate cancer. Bioconjug Chem. 2013;24(2):196–204. doi:10.1021/bc300473x.
94. Starmans LW, Hummelink MA, Rossin R, Kneepkens EC, Lamerichs R, Donato K, et al. Zr- and Fe-labeled polymeric micelles for dual modality PET and T-weighted MR imaging. Adv Healthc Mater. 2015. doi:10.1002/adhm.201500414.
95. Yamamoto F, Yamahara R, Makino A, Kurihara K, Tsukada H, Hara E, et al. Radiosynthesis and initial evaluation of (18)F labeled nanocarrier composed of poly(L-lactic acid)-block-poly(sarcosine) amphiphilic polydepsipeptide. Nucl Med Biol. 2013;40(3):387–94. doi:10.1016/j.nucmedbio.2012.12.008.
96. Lux J, Chan M, Elst LV, Schopf E, Mahmoud E, Laurent S, et al. Metal chelating crosslinkers form nanogels with high chelation stability. J Mater Chem B Mater Biol Med. 2013;1(46):6359–64. doi:10.1039/C3TB21104E.
97. Lux J, White AG, Chan M, Anderson CJ, Almutairi A. Nanogels from metal-chelating crosslinkers as versatile platforms applied to copper-64 PET imaging of tumors and metastases. Theranostics. 2015;5(3):277–88. doi:10.7150/thno.10904.
98. Black KC, Wang Y, Luehmann HP, Cai X, Xing W, Pang B, et al. Radioactive 198Au-doped nanostructures with different shapes for in vivo analyses of their biodistribution, tumor uptake, and intratumoral distribution. ACS Nano. 2014;8(5):4385–94. doi:10.1021/nn406258m.
99. Zhao Y, Sultan D, Detering L, Cho S, Sun G, Pierce R, et al. Copper-64-alloyed gold nanoparticles for cancer imaging: improved radiolabel stability and diagnostic accuracy. Angew Chem Int Ed Engl. 2014;53(1):156–9. doi:10.1002/anie.201308494.
100. Liu TW, Macdonald TD, Jin CS, Gold JM, Bristow RG, Wilson BC, et al. Inherently multimodal nanoparticle-driven tracking and real-time delineation of orthotopic prostate tumors and micrometastases. ACS Nano. 2013;7(5):4221–32. doi:10.1021/nn400669r.
101. Heng BC, Zhao X, Xiong S, Ng KW, Boey FY, Loo JS. Cytotoxicity of zinc oxide (ZnO) nanoparticles is influenced by cell density and culture format. Arch Toxicol. 2011;85(6):695–704. doi:10.1007/s00204-010-0608-7.
102. Osmond MJ, McCall MJ. Zinc oxide nanoparticles in modern sunscreens: an analysis of potential exposure and hazard. Nanotoxicology. 2010;4(1):15–41. doi:10.3109/17435390903502028.
103. Zhou J, Xu NS, Wang ZL. Dissolving behavior and stability of ZnO wires in biofluids: a study on biodegradability and biocompatibility of ZnO nanostructures. Adv Mater. 2006;18:2432–5.
104. Lee CM, Jeong HJ, Kim DW, Sohn MH, Lim ST. The effect of fluorination of zinc oxide nanoparticles on evaluation of their biodistribution after oral administration. Nanotechnology. 2012;23(20):205102. doi:10.1088/0957-4484/23/20/205102.
105. Hong H, Wang F, Zhang Y, Graves SA, Eddine SB, Yang Y, et al. Red fluorescent zinc oxide nanoparticle: a novel platform for cancer targeting. ACS Appl Mater Interfaces. 2015;7(5):3373–81. doi:10.1021/am508440j.
106. Shi H-Y, Deng B, Zhong S-L, Wang L, Xu A-W. Synthesis of zinc oxide nanoparticles with strong, tunable and stable visible light emission by solid-state transformation of Zn (II)-organic coordination polymers. J Mater Chem. 2011;21(33):12309–15.